Nanoscale

Accepted Manuscript

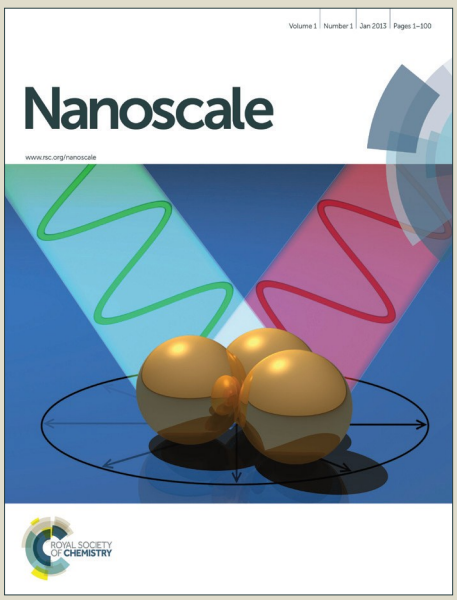

ROYAL SOCIETY OF CHEMISTRY

www.rsc.org/nanoscale

Nanoscale

ARTICLE

Tuning and predicting the wetting of nanoengineered material surface

Received 00th November 2015,
Accepted 00th January 2016

DOI: 10.1039/x0xx00000x

www.rsc.org/

M. Ramiasa-MacGregor[a#], A. Mierczynska[b#], R. Sedev[a] and K.Vasilev[c*]

The wetting of a material can be tuned by changing the roughness on its surface. Recent advances in the field of nanotechnology open exciting opportunities to control macroscopic wetting behaviour. Yet, the benchmark theories used to describe the wettability of macroscopically rough surfaces fail to fully describe the wetting behaviour of systems with topographical features at the nanoscale. To shed light on the events occurring at the nanoscale we have utilised model gradient substrata where surface nanotopography was tailored in a controlled and robust manner. The intrinsic wettability of the coatings was varied from hydrophilic to hydrophobic. The measured water contact angle could not be described by the classical theories. We developed an empirical model that effectively captures the experimental data, and further enables us to predict wetting of surfaces with nanoscale roughness by considering the physical and chemical properties of the material. The fundamental insights presented here are important for the rational design of advanced materials having tailored surface nanotopography with predictable wettability.

Introduction

It is well established that the wettability of a material can be tuned by changing the roughness of its surface [1-6]. Consequently, tailoring surface roughness could become a powerful tool to effectively enhance wetting-related processes [7]. Two well-established models (Cassie and Wenzel models) are generally effective at describing wetting behaviour on substrates with significant microscale surface roughness. However, many advanced processes and applications deal with topographic features at the nanoscale which are poorly addressed in existing models. The rapid developments in the fields of nanotechnology and nanofabrication demand a deeper understanding and the capacity to predict how nanoscale surface topography can be used to tailor surface wettability.

The two distinct classic wetting theories express the contact angle measured on a rough surface, θ, as a function of the Young contact angle [8] (the equilibrium contact angle on a chemically uniform and ideal smooth surface), θ_Y. In the Wenzel model [9] it is assumed that water conforms to the surface topography and θ is given by :

$$cos\theta = rcos\theta_Y \quad (1)$$

where r is a roughness factor defined as the ratio between the real surface area, A, and the geometric projected area of the rough surface, A_0. Since r is always greater than unity, this model predicts that surface roughness enhances the hydrophobicity of an inherently hydrophobic surface ($\theta_Y > 90°$), while a hydrophilic solid ($\theta_Y < 90°$) will become more hydrophilic ($\theta < \theta_Y$) as its roughness increases. This type of wetting state is depicted in Figure 1a with the example of spaced surface grooves, a topography typically resulting in a Wenzel configuration. The Cassie model applies where the formation of air pockets within the substrate asperities is energetically favourable [10]. The resulting composite surface consists of well-defined domains of trapped air and solid surface with respective area fractions ϕ_v and ϕ_s ($\phi_v = 1 - \phi_s$). Assuming that the water-air contact angle is 180°, the apparent contact angle is given by

$$cos\theta = -1 + \phi_s(\cos\theta_Y + 1) \quad (2)$$

Air trapping naturally occurs for water spreading on highly hydrophobic (e.g. fluoro-based coating with large θ_Y), and very rough surfaces ($r \gg 1$) [3, 7, 11, 12]. A typical Cassie wetting state is pictured in Figure 1b with the example of tall pillars with high surface density. Elaborate experimental and modelling studies have however highlighted limitations to these benchmark theories. For instance, they only apply for homogeneous surface roughness, that is when the dimension of the droplet is significantly larger than that of the surface features (typically more than 3 order of magnitude).[13] Also, Wenzel and Cassie models do not account for the effect of contact line pinning which can result in mixed wetting states due to local energy minima. [14, 15] Indeed, transitions between Cassie and Wenzel states can theoretically occur for moderate surface roughness (r< 1.7 [16]) and moderate hydrophobicity ($\theta_Y \sim 90°$). Though, these intermediate situations are complex and not fully understood [17]. For example, intrinsically hydrophilic surfaces can be made hydrophobic when air trapping occurs in spite of

[a] Future Industries Institute, University of South Australia, Mawson Lakes, SA 5095, Australia.
[b] Australian Wine Research Institute, Waite Precinct, Hartley Grove corner Paratoo Road, Urrbrae SA 5064, Australia.
[c] School of Engineering, University of South Australia, Mawson Lakes, SA 5095, Australia.
# Equal contribution.

Electronic Supplementary Information (ESI) available Detailed characterization of the nanorough substrates and model derivation are provided in supporting information. See DOI: 10.1039/x0xx00000x

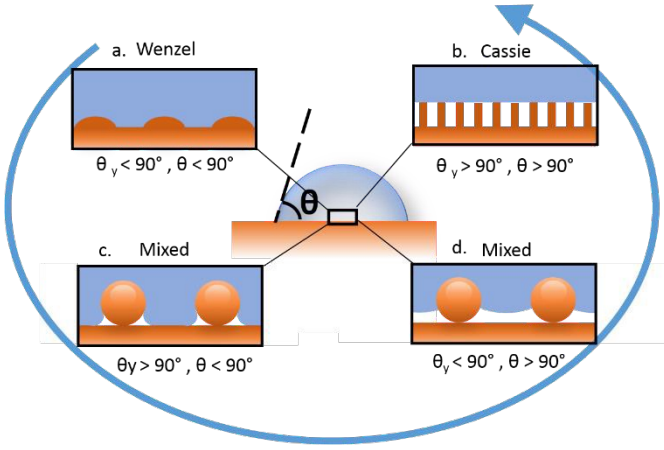

Figure 1. Different possible microscopic wetting states of the solid-liquid interface. (a) Wenzel state, intimate conformal solid-liquid contact (b) Cassie State, maximum air trapped between the solid and the suspended liquid phase (c) case of mixed wetting states achievable with re-entrant geometry where the liquid phase penetrate the capillary pore to touch the base of the substrate only trapping limited amount of air underneath the topographical overhangs (d) case of mixed wetting states achievable with re-entrant geometry where the liquid phase penetrates below the onset of the overhangs but remain suspended between the defects.

an unfavourable energy balance [5, 18, 19]. This type of mixed wetting states are sketched in Figure 1c and 1d, for a surface endowed with spherical features moderately spaced, where small or large air pocket are trapped within the topography respectively. An extended version of the Cassie equation [20, 21] was used to demonstrate that such metastable Cassie state are possible when the shape of the surface roughness promotes strong contact line pinning [22-24], e.g. when the maximum defect slope is larger than 90° [23, 25]:

$$cos\theta = -1 + \phi_s(r_{\phi_s}\cos\theta_Y + 1) \quad (3)$$

In equation (3), the wet area, ϕ_s, is determined geometrically from the substrate topographical profile and r_{ϕ_s} is its roughness factor.

Micrometric re-entrant geometry have been used to engineer omniphobic surfaces, capable to repel liquids with very low surface tension [24]. Interestingly enough though, little attention has been paid to nanosize features. Indeed, for several decades, it has been commonly assumed that RMS roughness smaller the 100 nm would not affect the static wettability of a solid substrate [26-31]. Modern studies, however, have proven that the shape of surface nanodefects and their density have a strong impact on wetting behaviour, and so even when the overall RMS value is below 100 nm [1, 4, 5, 11, 32-34]. The general consensus arising from these studies is that Wenzel and Cassie models fail to fully describe the wetting behaviour for systems with nanoscale topography [35]. Indeed, when the surface texture goes down to the nanoscale, thermodynamic considerations become, alone, insufficient to describe substrate wettability because multiple other forces capable to create metastable states become significant (e.g. line tension [36], thermal fluctuation [33, 34], capillary pressure [5], and other adhesion forces [29, 37, 38]).

As the field of material nanofabrication develops, it is now crucial to understand the impact of surface nanotopography on the contact angle experimentally observed on nanorough substrates. Undeniably, from a practical point of view, nanostructured surfaces present significant advantages compared to their micro-textured counterpart [39, 40]. For example, superhydrophobic behaviour can be achieved from nano-features alone [41], with the advantage that surfaces with textures smaller than 100 nm are more robust than microtextured ones and display remarkable optical properties such as transparency [7, 42], tuneable reflectance [43], super transmissivity [44]. With these assets nanostructured surfaces are on their way to become the new materials of choice for use in photovoltaics, optical sensors, aeronautics, MEMS and other applications.

In order to fully exploit the opportunities offered by nanotextured surfaces, we need to understand and be able to model and predict their wetting behaviour. To address these challenges we engineered controlled surface gradients of nanotopographical features size and density. We have also uniquely tailored the outermost surface chemistry in order to control the intrinsic surface wettability. Our results defy the prediction of Wenzel and Cassie models, confirming the complex wetting behaviour instigated by nanoscale surface defects. Furthermore we developed a model capable of predicting the experimental contact angle based on the surface intrinsic wettability and the density of spherical nano-features. Our experimental results and model show how, using a re-entrant surface geometry, the static contact angle of water can be tailored to suit specific applications by changing the surface nanofeature density and/or coating chemistry.

Results and discussion

Model nanoengineered surfaces.

To generate controlled surface nanotopography, gold nanoparticles of three different sizes (16, 38 or 68 nm) were immobilised along a sample in an increasing number density (*n*) manner using a method that we have reported previously [45]. The number of particles increases along the × axis as visualised by the AFM images in Figure 2a. To tailor the outermost surface chemistry of the material these nanotopography gradients were overcoated with a 5 nm thin plasma deposited films using as precursors acrylic acid (ppAc), allylamine (ppAA) and 1,7-octadiene (ppOD). These precursors result in coatings with distinct and targeted intermediate levels of wettability: mildly hydrophobic, moderately hydrophobic and hydrophobic, respectively [46, 47]. The thickness of the plasma polymer coating was carefully adjusted to 5 nm since we know that this thickness is sufficient to provide a continuous and pinhole free coating along the entire surface but allows for presenting the original nanotopography [45, 48], as schematically depicted in Figure 2b. These gradient surfaces are excellent model substrata where the surface chemistry is constant and tailored and the surface nanotopography varies in spacing and magnitude.

The water contact angles on the smooth ppAc, ppAA and ppOD surfaces, θ_o, are shown in Figure 2c. The acrylic and amine coatings are less hydrophobic due to the presence of polar amine and carboxylic groups, respectively. The octadiene coating is the most hydrophobic one because it exposes mainly

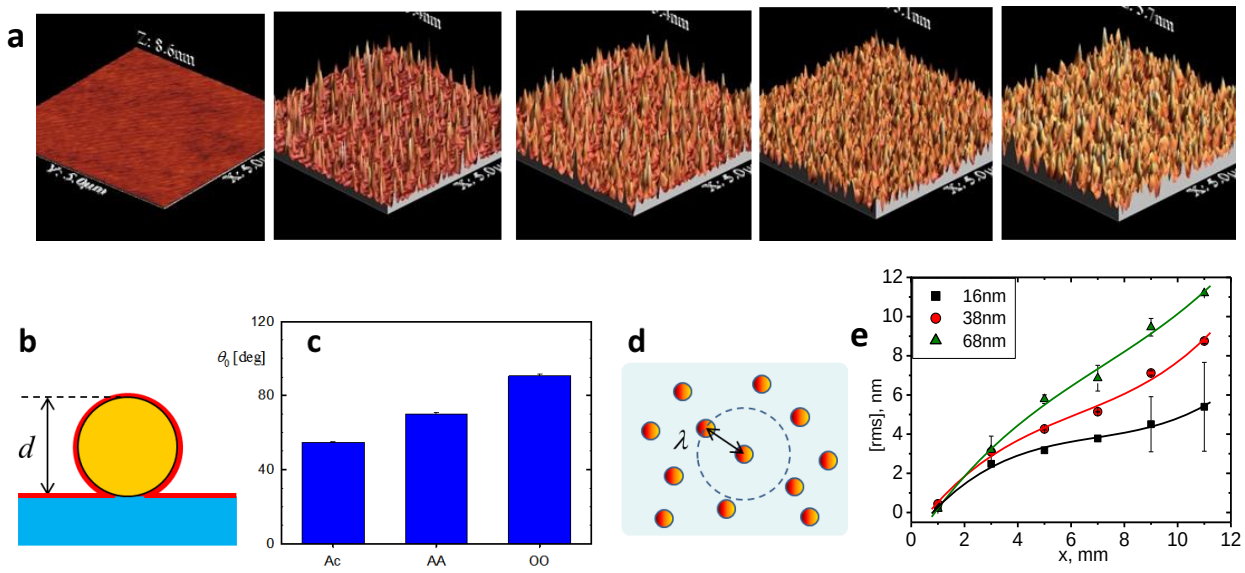

Figure 2. Physico-chemical characterisation of the model nanorough substrates. (a) Gold nanoparticles (diameter 16 nm). The number of particle per unit area, n, increases along the gradient x, i.e. left to right. (b) Schematic of a Gold nanoparticle plasma coated with a thin polymer layer. (c) Advancing water contact angles on smooth coatings of acrylic acid (ppAc), allylamine (ppAA), and octadiene (ppOD). (d) Definition of the average interparticle distance, λ. (e) RMS roughness values for the three different particles size over the length of the topographical gradient.

methylene groups to the wetting liquid. As the number of particles per unit area, *n*, increases along the sample (*x* increasing), the particles are located closer to each other but do not overlap, i.e. no multilayer, is formed (Figure 2a). Therefore, for a given particle size, surface roughness is directly related to the average distance between two particles, λ (Figure 2d). Care was taken so that the variation of *n* was the same for the three different particle sizes (see Figure SI.1 in supporting information)

The local surface roughness of the samples is determined by the diameter, *d*, and surface density, *n*, of the particles. The RMS roughness, R_{RMS}, increases with both the diameter and surface density of the particles, *n* (Figure 2e).

This also shows that, although the interparticle distance λ decreases along the gradient, it always remains significantly larger than the particles size (Figure SI2.b), thus confirming that a monolayer of particles is never exceeded. The average distance λ can also be regarded as the average size of the surface pores formed in between the nanoparticles. This average pore size varies between 100 and 800 nm. Finally, the particle surface coverage, $C = \pi d^2 n/4$, is very similar for all particle size. It increases approximately linearly along the surface gradient but is always relatively small, namely less than 5% (Figure SI2.c).

Substrates wettability.

The advancing water contact angles are shown in Figure 3 as functions of the position on the gradient surfaces. In all cases the contact angle increased with the particle coverage (*x* increasing). The contact angle measured on the smooth most hydrophobic coating (ppOD, Figure 3c) is obtuse (θ_o=95°) and it increases as surface roughness increases with the position *x*.

Figure 3. Static advancing contact angle results. Variation of the advancing water contact angle along the surface gradient (position x) for the 3 nanoparticle size, 16nm in blue, 38nm in green and 68nm in red. (a) Hydrophilic acrylic acid coating ppAC, (b) moderately hydrophilic allylamine coating ppAA, and (c) Hydrophobic octadiene ppOD. In all panels, the dashed line represent Wenzel's predictions as per equation (1), where, r = 1 + πd²n and θ_Y approximated to the experimental value of the contact angle measured on the smooth substrate.

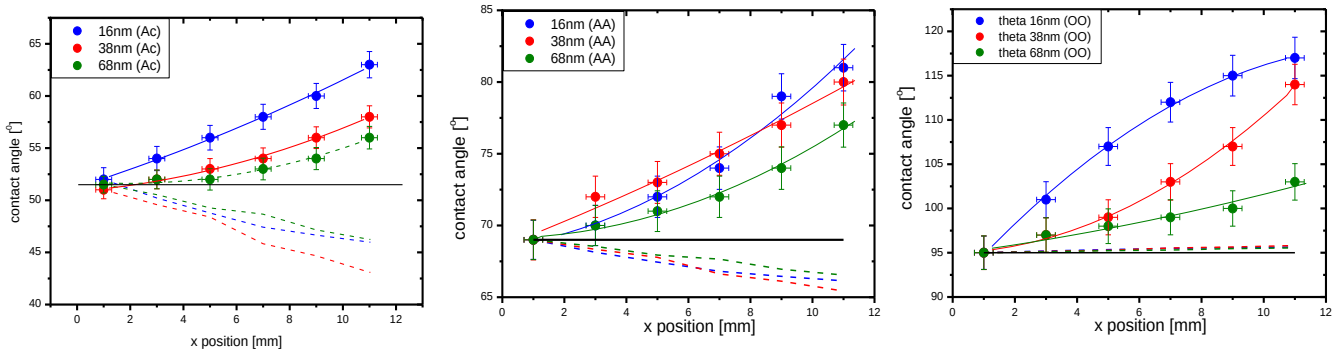

This could be a Wenzel type behaviour where the increasing roughness (through the Wenzel factor *r*) increases the apparent contact angle according to Equation (1). However, the Wenzel ratio *r* (easily estimated as r = 1 + πd²n), does not exceed 1.2 and therefore Wenzel's equation predicts an insignificant increase of the contact angle (a total change of about a degree, as shown by the dash lines in Figure 3c). Instead, as particles are getting closer (at larger *x*) the effective size of the surface pores, λ, diminishes. Since the ppOD coating is intrinsically hydrophobic one may expect pockets of air to be formed where neighbouring particles form a hydrophobic pore which is too small to be penetrated by the water at atmospheric pressure. In other words a Cassie wetting state may be achieved locally. In this case, and since the effective contact angle of water on air is 180°, an increase in the apparent contact angle measured on the gradient surface is expected. However, if the whole liquid-solid interface was in the Cassie state (as depicted in Figure 1.b.) one would estimate through equation (2), with $\phi_s = C$, an apparent contact angle of over 160°, i.e. the surface would behave like a superhydrophobic one. From the results shown in Figure 3c, one can see that this is clearly not the case: the contact angles measured never exceed 117°. Therefore the wetting state must consist of mixed domains of intimate solid-liquid contact (Wenzel state) and Cassie domains where small bubbles are trapped between the solid and the liquid.

We now return to the contact angles measured on the other two coatings (Figures 3a and 3b). In both cases the water contact angles on the smooth surfaces are acute (51° and 69°, for acrylic acid and allylamine coating respectively) and so Wenzel model would predict a decrease in contact angle with increasing surface roughness, as shown by the dash lines in Figure 3a and 3b. Therefore the significant contact angle increase observed in the experiments can only be explained by the formation of a partial Cassie state.

In cylindrical capillaries, the boundary between liquid penetration and liquid retention is exactly at 90° because the sign of the capillary pressure changes at that point. Therefore the Cassie state can be realised only with intrinsically hydrophobic coatings (θ > 90°). However, if the capillary size changes along the capillary then the slope of the capillary walls is changing and it is now possible for a Cassie state to be achieved even for three-phase systems with an acute contact angle as sketched in Figure 1d. The key requirement is for the surface features to have a re-entrant geometry that is a curvature such that the air gaps broaden toward the surface of the substrate. This is the case with the nanoparticles anchored on the gradient surfaces. Because the plasma coating is conformal (Figure 2b), as the liquid front penetrate the structure, the liquid-air interface need to increase. The energetically unfavourable creation of extra liquid-air interface balances the favourable wetting of the hydrophilic nanoparticle coating, thus allowing for a small area of liquid surface to be supported on top of a trapped air bubble. This phenomenon was evidenced by Tuteja et al. [24] for micro fibres and micron size "mushroom" shape pillars. In these systems, the aspect ratio of the pores created by the re-entrant micro-features, allows for the liquid to remain suspended in between defects, without reaching the base of the substrate (Figure 1.d). To the best of our knowledge the only report on wetting behaviour on nanoscale re-entrant geometry structure is the work of Munchi and co-workers [49] who found that, despite Wenzel prediction, the contact angle of a macroscopic water droplet on hydrophilic indium oxide nanoparticles on silicon surface increases with the nanoparticles size. An extended Young equation including line tension considerations was able to qualitatively depict the overall experimental data trend. However, non-negligible deviation from the theoretical prediction were found and attributed to significant variation in the nanoparticle areal density between the different nanoparticles size, a parameter that was not accounted for in that model. In the present work, however, the particle surface coverage has been quantified and its influence on the wetting state is investigated in the following section.

Figure 4. Estimation of the amount of air trapped in the mixed wetting state attained with the nanoparticle re-entrant geometry. (a) Liquid air fraction estimated using the modified Cassie equation (equation 3) and the experimental values of θ_Y and θ for all substrate investigated and plotted as a function of the nanoparticle surface coverage for all samples investigated. (b) Corresponding schematic representation of the small air bubble trapped under the particle overhangs for hydrophilic and hydrophobic coating.

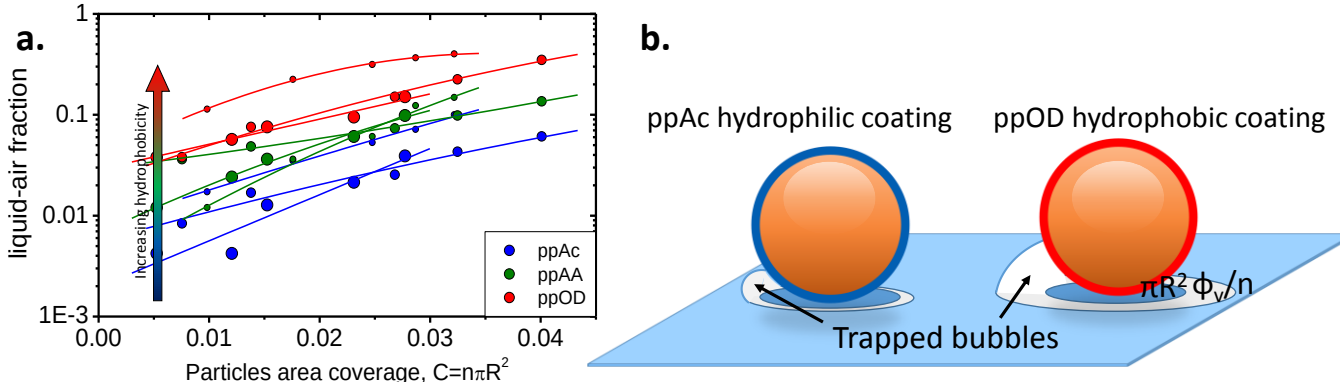

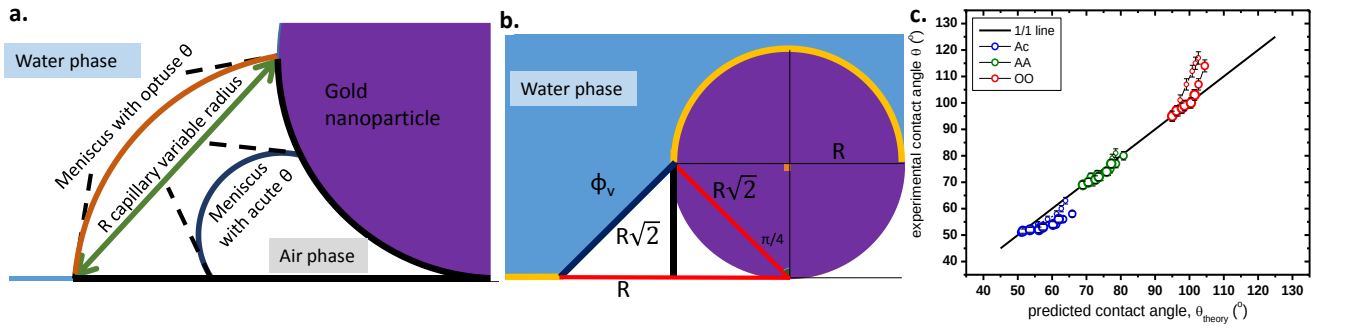

Figure 5. Schematic of the mixed wetting state achieved on the re-entrant nanotopographical features. (a) Schematic of the truncated cone capillary space present under and all around the overhang of the spherical nanoparticles, together with the possible meniscus shape predicted from the intrinsic plasma polymer wettabilities. (b) Geometrical model of the capillary space as considered for numerical derivation. Assuming a flat meniscus stopped at the entrance of the capillary space, the liquid-air fraction surface area, ϕv, is calculated as the lateral area of a truncated cone of base radius 2R, top radius R and lateral length R√2, φ_v=nπ3√2 R^2 (c) Comparison between the experimental contact angle measured on the whole range of substrate studied on the y axis, and, on the x axis, the contact angle values predicted from the proposed model, equation (7), using as input parameters only the nanoparticle radius, R, their surface density, n, and the contact angle on the corresponding smooth coating, θ.

Overall, in the experiments presented here, due to the re-entrant geometry of the plasma coated nanoparticles, the behaviour of the three coatings of different intrinsic wettability (ppAc – relatively hydrophilic, ppAA – less hydrophilic and ppOD – hydrophobic) is essentially similar. In all cases a mixed wetting state is formed with some air trapped within the surface nanoroughness.

Qualitative estimation of the mixed wetting state.

The extended Cassie equation, equation (3), is now used to evaluate what the actual liquid-air contact area fraction, ϕ_v, should be to account for the experimental values of θ measured along the nanorough gradient surfaces and θ_Y measured on the corresponding smooth surfaces:

$$\phi_v = 1 - \frac{cos\theta + 1}{r_{\phi_s}\cos\theta_Y + 1} \quad (4)$$

In this estimate we have used the total Wenzel factor, *r*, which is an overestimate of the actual r_{ϕ_s}, and we used the ϑ_o as an approximation of the young contact angle, i.e. 55°, 69° and 95° for ppAc, ppAA and ppOD coatings respectively. In Figure 4a, we plotted the fraction of air trapped for all different samples as a function of the nanoparticle surface coverage. The fraction of air trapped ranges from 1 to 40% over the range of substrates investigated, which is in all cases much less than what would be expected in a complete Cassie state (i.e. >95% due to the low nanoparticle coverage), thus confirming that the mixed wetting state achieved on these nanorough surfaces most likely consist of rather small air pockets trapped by the overhang of the nanoparticles, as depicted in Figure 1c.

The more hydrophobic the coating the more air is trapped (vertical arrow showing increasing hydrophobicity) and for a same surface coating, the trapped air fraction increases with the nanoparticles surface density, *n*. Although, for identical coating chemistry and surface coverage, the small particles initially appear more efficient at trapping air, normalisation of the trapped air fraction to the number of nanoparticles per unit area (ϕ_v/n), reveal that the larger particles actually trap more air as shown in Figure SI-2 .

In all cases the amount of liquid-air interface around each particle correspond to an area only slightly larger than the single particle projected surface area itself (Figure 4b) and is always much less than the average inter-particle area. Thus, unlike systems consisting of micro-sized re-entrant topography where the liquid is suspended between the defects, here the liquid appears to touch the base of the substrate between the nanodefects and only local air pockets remain trapped "under" the nanoparticles overhangs. It is also interesting to note that the amount of air trapped per particle remain rather constant with increasing particles coverage (Figure SI-3). This indicates that the amount of air trapped by individual nanoparticles is entirely governed by particle size (R) and intrinsic wettability (θ_Y).

Predictive model.

Since it appears that the pores created in between nanoparticles are penetrated until the substrate surface, we now propose a liquid penetration model considering the small capillary space created between the nanoparticles overhangs and the flat substrate as sketched in Figure 5a. These capillary do not have a standard cylindrical shape, but an intricate curved profile spanning all around the spherical particle base. As a first approximation, we model this capillary space as a truncated circular cone of summit angle π/4 as sketched in Figure 5b.

We further assume, for all coatings and particle size, that a flat meniscus is stopped at the entrance of these capillary cones. Under these assumptions we calculate the liquid-air fraction surface area, ϕ_v, as the lateral area of a truncated cone of base radius *2R*, top radius *R* and lateral length $R\sqrt{2}$ (Figure 5b),

$$\phi_v = n\pi 3\sqrt{2}\, R^2 \quad (5)$$

In this geometry, the Wenzel factor of the solid-liquid interface, r_{ϕ_s}, is:

$$r_{\phi_s} = \frac{1 - 2n\pi R^2}{1 - 3\sqrt{2}n\pi R^2} \quad (6)$$

And so the new wetting equation becomes, after simplifications (detailed derivation is available in supporting information),

$$cos\theta = \cos\theta_Y - n\pi R^2(3\sqrt{2} + 2\cos\theta_Y) \quad (7)$$

The contact angle obtained from this model is compared to the experimental data in Figure 5.c.

The very good agreement between the model and experimental data strongly supports our hypothesis of nano air bubbles trapped under the overhangs of the re-entrant nanoparticle geometry. However, one can notice a slight deviation from the

model occurring at high nanoparticle coverage. For the most hydrophobic substrate the model slightly underestimate the contact angle, indicating that the trapped air bubble and in turn the liquid-vapour surface area are larger than what was chosen in this model, as sketched in Figure 5a, orange meniscus. On the other hand, for the most hydrophilic substrate, the experimental contact angle is slightly smaller than predicted, here this indicates that the liquid must have penetrated further under the particle overhangs, and thus created a smaller liquid-air surface area, Figure 5a, blue meniscus. The mixed wetting state observed on the model nanorough surfaces studied here is the result of a complex equilibrium between capillary pressure and the resistance from the air confined under the spherical particle overhangs. This unique wetting state is achieved as a result of the limited penetration of water into the nanocapillary space formed under the spherical particles. This configuration is possible because the system has nanoscale dimensions, where gravitational effects are negligible and where the trapped air cavities form stable nanobubbles.[50-52] Due to the re-entrant nature of the geometry of the spherical nanoparticles the effect is seen with relatively hydrophilic systems (Ac and AA) but it is much stronger for the intrinsically hydrophobic OO coating. The empirical model provided here satisfactorily predicts the combined effect of anchored spherical nanoparticles (n and d) and intrinsic coating wettability (θ_Y) on the macroscopic wetting behaviour (θ) observed. This model could be used to guide the selection of surface nanoparticle density and coating wettability for a range of applications. Although, surface-bound nanoparticles constitute a common way to generate surface nanoroughness, many other nanogeometries are also used to confere tailored topographies. In its current form the proposed model is specific to the particular kind of spherical nanofeatures investigated. Nevertheless simple geometrical considerations can generally be implemented to estimate the volume of air trapped within features with different shape in order to adapt the reasoning followed in the present work to other type of nano-geometries.

Experimental

Materials.

Allylamine (AA) (98%, Aldrich), acrylic acid (AC) (99%, Aldrich), 1,7-octadiene (OD) (98%, Aldrich) sodium borohydrate (Aldrich), hydrogen tetrachloroaurate (99.9985%, ProSciTech), trisodium citrate (99%, BHD Chemicals, Australia Pty. Ltd.), 2-mercaptosuccinic acid (97%, Aldrich) were used as received. For solution preparation and glassware cleaning, high purity water was used, produced by the sequential treatments of reverse osmosis, two stages of mix bed ion exchange, two stages of active carbon treatment, and a final filtering step through a 0.22 µm filter. The final conductivity was less than 0.5 µS/cm with a surface tension 72.8 mN/m at 20°C.

Plasma polymerization.

Plasma polymerization was carried out in a custom-built reactor described elsewhere using a 13.56 MHz plasma generator.[53] Deposition of allylamine (ppAA), acrylic acid (ppAC) and octadiene (ppOD) was carried out at a pressure of 0.2 mbar and a deposition time of 2 minutes. Power used for deposition of all three monomers was 40 W, 10 W and 20 W, respectively. Using these conditions polymer films of thickness 23 nm, 20 nm and 25 nm were obtained, respectively. A film of 5 nm thickness, used for overcoating, was achieved keeping a constant deposition time of 20 seconds for all monomers. Before deposition, all substrates were cleaned by applying air plasma for 2 minutes at 50 W.

Synthesis of gold nanoparticles (AuNPs).

AuNPs were synthesized by citrate reduction of $HAuCl_4$. Particles of ~ 38 nm diameter were synthesized from 150 ml of a 0.01 % boiling solution of $HAuCl_4$, to which 1.5 ml of a 1% solution of sodium citrate was added under vigorous stirring.[54] The solution was left to boil for 20 min and then allowed to cool to ambient temperature. The AuNPs were then surface modified with 2-mercaprosuccinic acid as in Zhu et al.[55] The particle diameters were confirmed via AFM imaging.

Gradients preparation.

The nanoparticles were gradually absorbed onto the functionalized amine substrates by controlled immersion into the solution of AuNPs as reported in Goreham et al [45]. The substrates were dipped gradually with a linear motion drive (Zaber T-LSR series), using Zaber software. After the required length was immersed (in this work 10 mm) the substrate was immediately retracted and thoroughly washed with Milli-Q water to remove all weakly bound particles. Rate of immersion was 5 mm/h, 2.5 mm/h and 1.66 mm/h 10 mm for the 16, 38 and 68 nm AuNPs, respectively.

Water contact angle measurements.

Sessile drop water contact angle was measured via Video Based Contact Angle Meter (OCA20, Dataphysics–Germany). Samples were affixed to a clean glass slide and droplet of MilliQ water was deposited onto the surface. A 2 µL droplet was formed at the end of a needle. The needle was lowered until the drop touched the surface and then retracted. The silhouette of the droplet was captured and imaged with a progressive scan CCD camera (JAI-CV-MOBX, Japan) and contact angles were determined by drawing the tangent close to the edge of the droplet using ImageJ software with the DropSnake plug-in [56]. The mean value of the contact angle was calculated from at least 5 individual measurements taken at different locations on the examined substrates. Experiments were conducted at 22ºC in a class-100 clean room.

X-ray Photoelectron Spectroscopy.

XPS analysis was used to determine the surface composition of the plasma polymer and the gradients of deposited AuNPs. XPS spectra were recorded on a Specs SAGE XPS spectrometer using Al Kα radiation source (hν = 1253.6 eV) operated at 10 kV and 20 mA. Elements present in a sample surface were identified from the survey spectrum recorded over the energy range 0–1000 eV at a pass energy of 100 eV and a resolution of 0.5 eV. The areas under selected photoelectron peaks in a widescan spectrum were used to calculate percentage atomic concentrations (excluding hydrogen). High-energy resolution

(0.1 eV) spectra were then recorded for pertinent photoelectron peaks at a pass energy of 20 eV to identify the possible chemical binding environments for each element. All the binding energies (BEs) were referenced to the C1s neutral carbon peak at 285 eV, to compensate for the effect of surface charging. The XPS analysis area was circular with a diameter of 0.7 mm. The processing and curve-fitting of the high-energy resolution spectra were performed using CasaXPS software.

Atomic Force Microscopy (AFM).

An NT-MDT NTEGRA SPM atomic force microscope (AFM) was used in non-contact mode to provide topographical images. Silicon nitride non-contact tips coated with Au on the reflective side (NT-MDT, NSG03) were used and had resonance frequencies between 65 and 100 kHz. The amplitude of oscillation was 10 nm, and the scan rate for 4 µm x 4 µm images was 0.5 Hz. The scanner used had a maximum range of 100 µm and was calibrated using 1.5 µm standard grids with a height of 22 nm.

Conclusions

We demonstrated experimentally the wetting behaviour of nanorough surfaces with different intermediate intrinsic wettability. This was achieved through model substrata where we were varied the density and size of nanoparticles and uniquely tailored the outermost surface chemistry. A mixed wetting state is achieved and within the range of parameters examined the contact angle of water always increases with particle coverage. The effect is stronger for smaller particles and more hydrophobic coatings. The wetting behaviour at the nanoscale and intermediate surface chemistry does not obey established models. With the experimental data in hand we developed a model which allow us to understand the wetting behaviour of nanorough surfaces. Knowing the size and the surface density of the nanofeatures, as well as the contact angle on the chemically equivalent smooth surface, one can now estimate and predict the actual wettability of the nanotextured surface. This model opens opportunities for scientists and engineers to model and design of nanoengineered surface for advanced applications in various fields.

Acknowledgements

This research was supported under Australian Research Council's Discovery Projects funding scheme (project number DP110103391).

Notes and references

1. J. D. Miller, S. Veeramasuneni, J. Drelich, M. R. Yalamanchili and G. Yamauchi, *Polymer Engineering & Science*, 1996, **36**, 1849-1855.
2. J. Bico, C. Tordeux and D. Quéré, *Europhys. Lett.*, 2001, **55**, 214-220.
3. D. Quéré, *Annual Review of Materials Research*, 2008, **38**, 71-99.
4. P. Joseph, C. Cottin-Bizonne, J.-M. Benoit, C. Ybert, C. Journet, P. Tabeling and L. Bocquet, *Phys. Rev. Lett.*, 2006, **97**, 156104.156101-156104.156104.
5. C. Ran, G. Ding, W. Liu, Y. Deng and W. Hou, *Langmuir*, 2008, **24**, 9952-9955.
6. D. Bonn, J. Eggers, J. Indekeu, J. Meunier and E. Rolley, *Rev. Mod. Phys.*, 2009, **81**, 739-805.
7. A. Nakajima, K. Hashimoto and T. Watanabe, *Monatshefte für Chemie / Chemical Monthly*, 2001, **132**, 31-41.
8. T. Young, *Philos. Trans. R. Soc. London*, 1805, **95**, 65-87.
9. R. N. Wenzel, *The Journal of Physical and Colloid Chemistry*, 1949, **53**, 1466-1467.
10. A. B. D. Cassie and S. Baxter, *Transaction of the Faraday Society* 1944, **40**, 546-551.
11. J. L. Campbell, M. Breedon, K. Latham and K. Kalantar-zadeh, *Langmuir*, 2008, **24**, 5091-5098.
12. X. J. Feng and L. Jiang, *Adv. Mater.*, 2006, **18**, 3063-3078.
13. A. Marmur and E. Bittoun, *Langmuir*, 2009, **25**, 1277.
14. A. Shahraz, A. Borhan and K. A. Fichthorn, *Langmuir*, 2012, **28**, 14227-14237.
15. M. S. Bell, A. Shahraz, K. A. Fichthorn and A. Borhan, *Langmuir*, 2015, **31**, 6752-6762.
16. R. E. Johnson and R. H. Dettre, in *Contact Angle, Wettability, and Adhesion*, American Chemical Society, 1964, vol. 43, ch. 7, pp. 112-135.
17. J. Bico, U. Thiele and D. Quéré, *Colloids Surf. Physicochem. Eng. Aspects*, 2002, **206**, 41-46.
18. A. Marmur, *Langmuir*, 2004, **20**, 3517-3519.
19. A. Lafuma and D. Quéré, *Nature Materials*, 2003, **2**, 457-460.
20. N. A. Patankar, *Langmuir*, 2003, **19**, 1249-1253.
21. A. Marmur, *Langmuir*, 2003, **19**, 8343-8348.
22. S. Herminghaus, *EPL (Europhysics Letters)*, 2000, **52**, 165.
23. J. Wang, F. Liu, H. Chen and D. Chen, *Appl. Phys. Lett.*, 2009, **95**, 084104.084101-084104.084103.
24. A. Tuteja, W. Choi, J. M. Mabry, G. H. McKinley and R. E. Cohen, *Proceedings of the National Academy of Sciences*, 2008, **105**, 18200-18205.
25. J. Wang and D. Chen, *Langmuir*, 2008, **24**, 10174-10180.
26. A. W. Neumann and R. J. Good, *Journal of Colloid and Interfacial Science*, 1972, **38**, 341-358.
27. H. J. Busscher, A. W. J. van Pelt, P. de Boer, H. P. de Jong and J. Arends, *Colloids and Surfaces*, 1984, **9**, 319-331.
28. C. W. Extrand and Y. Kumagai, *Journal of Colloid and Interfacial Science*, 1997, **191**, 378-383.
29. C. W. Extrand, *Journal of Colloid and Interfacial Science*, 2002, **248**, 136-142.
30. J. D. Eick, R. J. Good and A. W. Neumann, *Journal of Colloid and Interfacial Science*, 1975, **53**, 235-238.
31. C. Huh and S. G. Mason, *Journal of Colloid and Interfacial Science*, 1977, **60**, 11-38.
32. R. Fetzer and J. Ralston, *The Journal of Physical Chemistry C*, 2011, **115**, 14907-14913.
33. M. Delmas, M. Monthioux and T. Ondarcuhu, *Phys. Rev. Lett.*, 2011, **106**, 136102.136101-136102.136104.
34. A. Prevost, E. Rolley and C. Guthmann, *Phys. Rev. Lett.*, 1999, **83**, 348-351.
35. G. O. Berim and E. Ruckenstein, *J. Colloid Interface Sci.*, 2011, **359**, 304-310.
36. J. Drelich and J. D. Miller, *Langmuir*, 1993, **9**, 619-621.

37. S. M. M. Ramos, E. Charlaix, A. Benyagoub and M. Toulemonde, *Physical Review E*, 2003, **67**, 031604.031601-031604.031606.
38. M. Ramiasa, J. Ralston, R. Fetzer, R. Sedev, D. M. Fopp-Spori, C. Morhard, C. Pacholski and J. P. Spatz, *J. Am. Chem. Soc.*, 2013, **135**, 7159-7171.
39. P. Kim, M. J. Kreder, J. Alvarenga and J. Aizenberg, *Nano Lett.*, 2013, **13**, 1793-1799.
40. A. Checco, A. Rahman and C. T. Black, *Adv. Mater.*, 2014, **26**, 886-891.
41. K. K. S. Lau, J. Bico, K. B. K. Teo, M. Chhowalla, G. A. J. Amaratunga, W. I. Milne, G. H. McKinley and K. K. Gleason, *Nano Lett.*, 2003, **3**, 1701-1705.
42. N. Wang and D. Xiong, *Colloids Surf. Physicochem. Eng. Aspects*, 2014, **446**, 8-14.
43. S. J. Cho, T. An, J. Y. Kim, J. Sung and G. Lim, *Chem. Commun.*, 2011, **47**, 6108-6110.
44. K.-C. Park, H. J. Choi, C.-H. Chang, R. E. Cohen, G. H. McKinley and G. Barbastathis, *ACS Nano*, 2012, **6**, 3789-3799.
45. R. V. Goreham, A. Mierczynska, M. Pierce, R. D. Short, S. Taheri, A. Bachhuka, A. Cavallaro, L. E. Smith and K. Vasilev, *Thin Solid Films*, 2013, **528**, 106-110.
46. K. Vasilev, A. Mierczynska, A. L. Hook, J. Chan, N. H. Voelcker and R. D. Short, *Biomaterials*, 2010, **31**, 392-397.
47. A. Mierczynska, A. Michelmore, A. Tripathi, R. V. Goreham, R. Sedev and K. Vasilev, *Soft Matter*, 2012, **8**, 8399-8404.
48. A. Michelmore, P. Martinek, V. Sah, R. D. Short and K. Vasilev, *Plasma Processes and Polymers*, 2011, **8**, 367-372.
49. A. M. Munshi, V. N. Singh, M. Kumar and J. P. Singh, *J. Appl. Phys.*, 2008, **103**, -.
50. P. Attard, *arXiv preprint arXiv:1503.04365*, 2015.
51. J. H. Weijs and D. Lohse, *Phys. Rev. Lett.*, 2013, **110**, 054501.
52. V. I. Melik-Gaikazyan, N. P. Emel'yanova and D. V. Dolzhenkov, *Russ. J. Non-ferrous Metals*, 2014, **55**, 309-317.
53. J. D. Whittle, D. Barton, M. R. Alexander and R. D. Short, *Chem. Comm.*, 2003, 2.
54. J. Turkevich, P. C. Stevenson and J. Hillier, *Discussions of the Faraday Society*, 1951, **11**, 23.
55. T. Zhu, K. Vasilev, M. Kreiter, S. Mittler and W. Knoll, *Langmuir*, 2003, **19**, 8.
56. M. D. Abràmoff, P. J. Magalhães and S. J. Ram, *Biophotonics international*, 2004, **11**, 36-42.